This article has been accepted for publication in a future issue of this journal, but has not been fully edited. Content may change prior to final publication.
Citation information: DOI: 10.1109/TVT.2025.3638699, IEEE Transactions on Vehicular Technology

Design of 2-Bit Circularly Polarized Reflectarray for Broadband Vehicle Communications

Fang Hu, Qiao Cheng, Lehu Wen, Wei Hu, *Senior Member, IEEE,* Xuekang Liu, Qi Luo, *Senior Member, IEEE*, and Steven Gao, *Fellow, IEEE*

***Abstract*—As an indispensable supplement to the terrestrial Internet of Vehicles (IoV), satellites provide a promising alternative for broad IoV coverage. To improve the broadband connection in satellite IoV service, this paper presents a novel broadband 2-bit circularly polarized (CP) reflectarray (RA). By analyzing the phasing characteristic of dual-loop unit cell, a -180° phase difference is achieved through a novel method of arranging resonances of the single loop and dual-loop. Owing to the wider phasing bandwidth of the dual-loop unit cell, -90° and -270° phase delays are obtained by changing the parameters of the dual-loop unit cell. The phase bandwidth of $70.5° \le |\phi| \le 109.5°$ is first-time introduced to characterize the AR bandwidth for the developed 2-bit unit cells. Therefore, compared to the traditional method focusing solely on the scaled size for reflective phase response, broadband AR and gain performances are obtained. Finally, as a performance demonstration, a planar RA composed of the developed 2-bit unit cells was fabricated and measured. Measured results confirm that broad 3dB gain bandwidth of 32% and 3dB AR bandwidth of 53% are achieved with high gain radiation, which show a good candidate for low-cost broadband and wide area coverage for satellite IoV service.**

***Index Terms*—Broadband, circular polarization, Internet of Vehicles (IoV), satellite, reflectarray.**

I. Introduction

THE emerging Internet of Vehicles (IoV) is a revolutionized technology that can not only enable us exchanging real-time information between users and fast-moving vehicles, but also provide high speed communication for users on vehicles [1]. As shown in the typical vehicle communication scenarios in Fig. 1, there are different types of vehicles, typically ships, planes, cars, requiring massive IoV connections. One we might notice that different from cars utilizing terrestrial-based communication networks, currently one feasible solution for voyaging ships and flying planes is utilizing the space-borne satellite communication networks. Therefore, satellite-based IoV networks provide an effective and alternative supplement to the terrestrial communications, pursuing ubiquitous connections for these underpopulated remote rural area, desert, ocean, and high altitude flying [2].

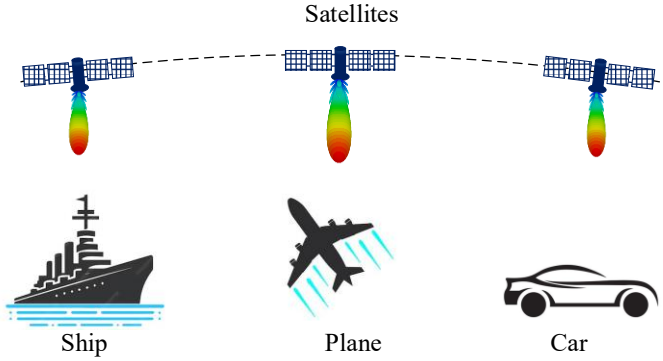

Fig. 1. Typical application scenarios of the satellite-based vehicle communications.

Recently, many cutting-edge antenna techniques [3]-[9] have been proposed and applied in IoV to achieve broadband, low-latency, and high throughput connection for vehicles. First to obtain broad bandwidth for vehicle communications, dipole antenna [3], dielectric antenna [4], are slot antenna [5]-[6] are developed and mounted on top of the cars for low-latency between vehicles. However, due to the effect of relatively large profile, these antennas have either the tilted radiation patterns or instable gains. To achieve stable connection between vehicles, antennas with stable and high gain unidirectional radiation are much favorable [7]-[9]. By using H-plane substrate integrated waveguide horn in [7], improved gain of 1.1 dB is obtained for mmWave vehicle communications. With the introduction of right-hand and left-hand phase shifters, unidirectional and orthogonal polarizations are achieved in [9] with stable and symmetrical radiation patterns. However, it is found that in these designs, most antennas are designed for the terrestrial IoV communication systems, which could not be directly used in satellite IoV systems.

To better accommodate satellite communication in IoV service, first antennas are normally designed in circular polarized (CP) radiation, owing to the advantage of its innate polarization immunity to the polarization angle between the transmitting antenna and the receiving antenna [10]. In addition,

This work was supported by Brunel Research Initiative and Enterprise Fund (BRIEF) and in part by HORIZON-MSCA-2022-SE-01 under Grant 101131204.. *(Corresponding author: Lehu Wen.)*

F. Hu, Q. Cheng, and L. Wen are with the Department of Electronic and Electrical Engineering, Brunel University London, Uxbridge, UB8 3PH, U.K. (E-mail: LehuWen@ieee.org)

W. Hu is with the National Key Laboratory of Antennas and Microwave Technology, Xidian University, Xian, 710071, China.

Xuekang Liu is with the School of Engineering and Digital Arts, University of Kent, Canterbury, CT2 7NT, U.K. (E-mail: XuekangLiu@ieee.org)

Q. Luo is with the School of Physics, Engineering and Computer Science, University of Hertfordshire, Hatfield, AL10 9AB, UK.

S. Gao is with the Department of Electronic Engineering, The Chinese University of Hong Kong, Hong Kong.

For the purpose of open access, the author(s) have applied a Creative Commons Attribution (CC BY) license to any Accepted Manuscript version arising.

to realize high gain CP radiation for satellite IoV communications, multi-layered printed patches [11]-[12], magnetoelectric dipole [13], aperture [14], and slot [15] are utilized as radiation elements. These designs have the features of high integration and high gain CP radiation. However, because of the multi-layered PCB technology, complex structures, narrow bandwidths, complicated feed design, and increased fabrication cost are the main challenges in these designs. For satellite IoV applications, in addition to the commonly required broadband bandwidths in impedance and CP radiation, arrays are always required with low cost, light weight, and easy integration.

Owing to such advantages in planar array aperture, low fabrication cost, simple spatial feed, and same high gain and broadband radiation, CP reflectarray (RA) antenna is another promising alternative for satellite IoV applications. The commonly used methods can be techniques of using phase delay line [16]-[18] and element rotation methods [19]-[21]. In [19], by using elliptic S-shaped patches, a very broad 2:1 CP bandwidth is achieved for the developed elements. However in this method, achieving a compact broadband CP antenna with stable radiation performance as the feed source is not as easy as the linearly polarized (LP) antenna. Therefore, different types of LP-CP RAs are designed for CP radiation [22]-[28]. The basic principle is that the elements in the surface aperture work as phase changeable LP-CP polarizers, so that an LP incident wave will be transformed into a CP reflective wave, and further be phased for high gain CP radiation, which can significantly simplify the design of feed antenna.

In this work, to achieve broadband satellite connection in IoV service and also to simplify array and feed design, a low-cost planar broadband CP reflectarray is proposed based on a new combination of novel 2-bit LP-CP unit cells. A -180° phase delay is firstly introduced from the phase difference between the dual-loop unit cell and single loop unit cell. Equivalent circuits of the single loop and dual-loop unit cells are analyzed to illustrate the inner phasing principle. In addition, -90° and -270° phase delays are obtained by elaborately changing the parameters of the dual-loop unit cell. Furthermore, phase bandwidth of $70.5° \le |\phi| \le 109.5°$ is firstly introduced to characterize CP bandwidth of LP-CP unit cells for planar array design. Therefore, broadband gain and AR performances are obtained for the developed CP RA. Both simulated and measured results demonstrate an excellent broadband performance of the developed RA, which is a good candidate for broadband and wide-area satellite IoV applications.

II. Principle of 2-Bit Phasing

In this section, a novel method of using single loop and dual loop structures is presented to realize broadband 2-bit reflection phases. Then, a new method to characterize the CP bandwidth by utilizing the reflection phase range of [70.5°, 109.5°] is proposed to underpin the design of broadband satellite RA, which will be used for non-reconfigurable 2-bit phasing in a broadband fixed beam CP RA design later.

A. Phasing Scheme

Fig. 2 shows the structures of the single-loop and coupled dual-loop in a square unit cell. Here, the single-loop shown in Fig. 2 (a) will be utilized to realize 0 reflection phase, while the dual-loop in Fig. 2 (b) will be utilized to realize -90, -180, and -270 reflection phases. Fig. 2 (c) shows the side view of the unit cell. The conductor etched on the top layer of the substrate is shown in pink colour, while the conductor etched on the bottom layer is shown in blue colour. Note that Rogers 4003C substrate with the relative permittivity of 3.55 and thickness of 0.508 mm is used in the unit cell design.

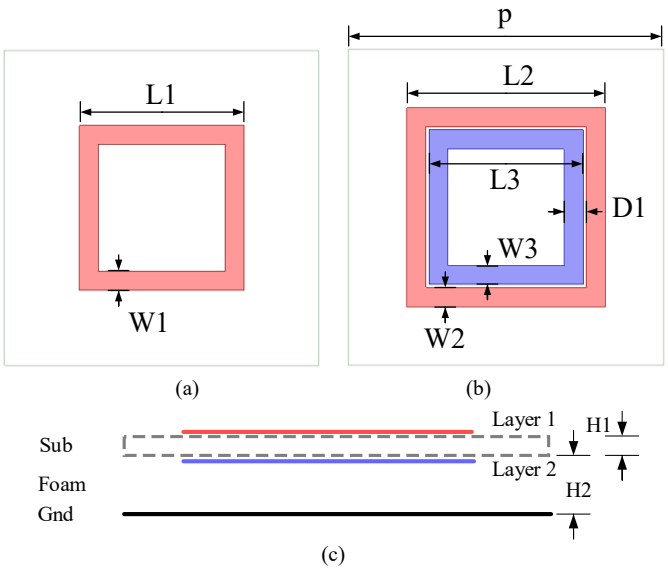

Fig. 2. Structures of (a) single square-loop and (b) coupled dual-loop in the unit cell. (c) Side view of the structures. (Parameters of the structure in simulation: p=10 mm, L1=5.2 mm, W1=W2=W3=0.6 mm, L2=4.9 mm, D1=0.7 mm. H1=0.508 mm, H2=3 mm.)

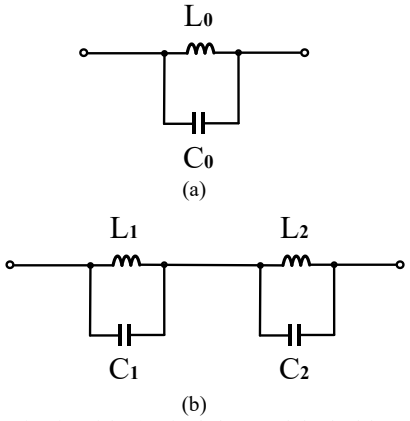

Fig. 3. Equivalent circuits of the (a) single loop and (b) dual-loop in the unit cell. (Component values in the circuits: L_0=0.47 nH, C_0=0.54 pF, L_1=0.2 nH, C_1=0.97 pF, L_2=0.45 nH, C_2=0.87 pF.)

To theoretically illustrate the magnitude and phase response of the two unit cells, the equivalent circuits are given and shown in Fig. 3. Because of the single loop in the unit cell, it can be equivalent as a simple shunt-circuit, and shown in Fig. 3 (a). Its input impedance then can be calculated as

$$Z_{in}^{a} = j\omega L_0 \,||\, \frac{1}{j\omega C_0} \tag{1}$$

and the resonant frequency in this unit cell is

$$f_0 = \frac{1}{2\pi\sqrt{L_0 C_0}} \tag{2}$$

The equivalent circuit of the dual-loop unit cell is shown in Fig. 3 (b). The input impedance is

$$Z_{in}^{b} = j\omega L_1 \,||\, \frac{1}{j\omega C_1} + j\omega L_2 \,||\, \frac{1}{j\omega C_2} \tag{3}$$

There as two resonances in the unit cell.

$$f_1 = \frac{1}{2\pi\sqrt{L_1 C_1}} \tag{4a}$$

$$f_2 = \frac{1}{2\pi\sqrt{L_2 C_2}} \tag{4b}$$

Based on the above equations, the reflection coefficients of the two unit cells can be calculated. First, the reflection coefficients of the two unit cells are obtained and shown in Fig. 4. The simulated results are also included in the figure for comparison. For the single loop unit cell shown in Fig. 4 (a) at the resonant frequency of 10 GHz, the reflection phase is 0 degree. For the dual-loop unit cell, two resonant frequencies can be expected, one is at 8 GHz, and the other is at around 11.5 GHz. The phases of both two resonant frequencies are 0 degree. In the figure, it is found that a reasonable agreement can be achieved between the calculated phase responses and the simulated phase responses, even though the equivalent circuits are simple.

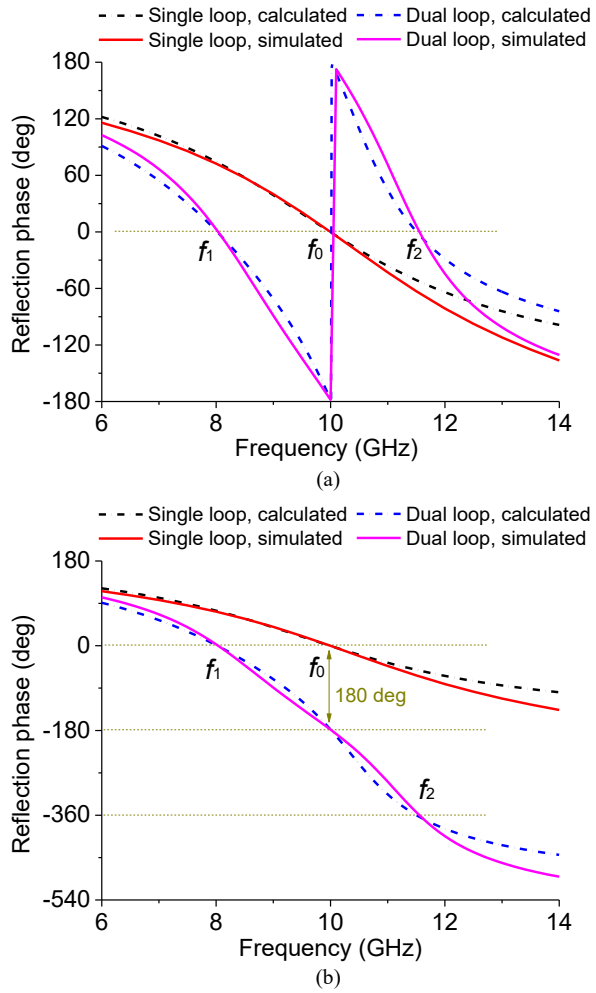

Fig. 4. (a) Reflection phases of the single loop and dual-loop. (b) Unwrapped form of the phases.

To facilitate observing the phase response within the bandwidth, the reflection phase of the unit cell is always shown in an unwrapped form just as shown in Fig. 4 (b). In this figure, we can see clearly the reflection phase range of the dual-loop is much larger than the single loop. For the single loop unit cell, the phase range is within [-180, 180], whereas the phase range for the dual-loop unit cell is within [-540, 180]. By elaborately locating two resonant frequencies of the dual-loop, an out-of-phase (180°) delay can be achieved between these two unit cells. One can also see the differences between the calculated and the simulated phase responses, especially for the frequencies in the upper frequency band. This is due to the overlook of the losses and the complex distributed coupling between the loops in the unit cells. Nonetheless, the simplified equivalent circuits are enough to illustrate the reflection characteristic of the unit cells.

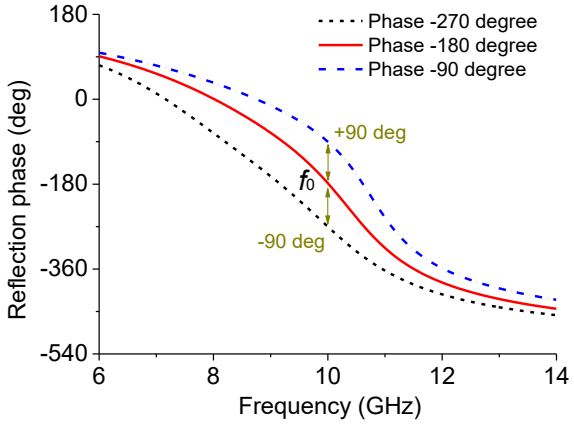

Fig. 5. Calculated reflection phases of the dual-loop unit cell by slightly changing the resonant frequencies.

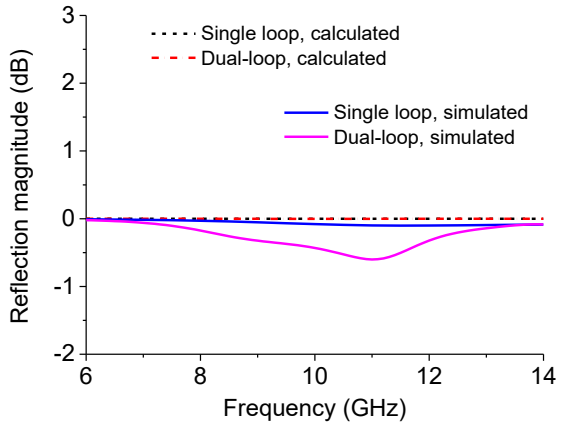

Fig. 6. Reflection magnitudes of the single loop and dual-loop unit cells.

Because there are two resonances in the dual-loop unit cell, this normally features wide reflection bandwidth compared to the single loop unit cell. Therefore, reflection phases of -90° and -270° can be achieved by slightly moving the resonances (or reflection bandwidth) of the dual-loop unit cell. Fig. 5 shows the calculated phase responses of the dual-loop unit cell under three types of different resonances. For -90° reflection phase at 10 GHz, the lumped element values in the equivalent circuit are L_1=0.2 nH, C_1=1 pF, L_2=0.45 nH, C_2=1 pF. For -270° reflection phase at 10 GHz, the lumped element values are L_1=0.2 nH, C_1=0.8 pF, L_2=0.45 nH, C_2=0.73 pF. As can be seen

in the figure, -90° and -270° reflection phases are achieved by using this method.

The reflection magnitudes of the two unit cells are also investigated and shown in Fig. 6. It can be seen that for the calculated results of the equivalent circuits, the reflection coefficients are ideal and close to 0. Because of the inclusion of the substrate loss and conductor loss in EM simulation, the obtained reflection magnitudes are lower than the calculated results, especially for the simulated result of the dual-loop unit cell. Because of the influence of the substrate and conductor losses in the unit cell, the simulated minimum reflection magnitude of -0.6 dB is observed within the bandwidth. Overall, the reflection is very strong and can be utilized for the design of the reflective unit cells.

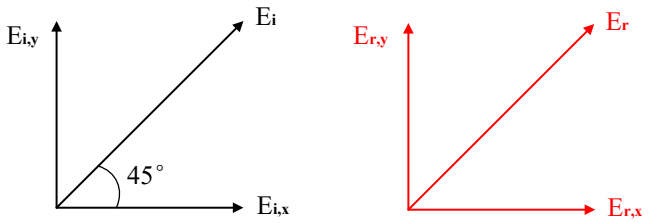

Fig. 7. Excitation method of the unit cell for CP radiation.

B. *Phase Characterization for Circular Polarization*

In this work, we will use a 45°-inclined line-incident planar wave to excite the LP-CP unit cells, this method can simplify the design of the array and feed for satellite IoV application. A phase bandwidth will be derived as the baseline for developing broadband LP-CP unit cells, so that frequency domain response of the unit cells can be characterized in pursuit of broadband CP radiation.

Fig. 7 shows the excitation method of the unit cell for CP radiation. It is known that for a 45°-inclined line-polarized incident E-field E_i, it can be resolved into two orthogonal directions.

$$E_i = E_{i,x}\hat{x} + E_{i,y}\hat{y} \tag{5}$$

where $E_{i,x} = E_{i,y}$.

The reflected E-field E_r by a reflective unit cell can also be resolved into two orthogonal components,

$$E_r = E_{r,x}\hat{x} + E_{r,y}\hat{y} \tag{6}$$

If we can achieve the below relations from the reflected field,

$$|E_{r,x}| = |E_{r,y}| = 1 \tag{7a}$$

$$\text{and} \quad \angle E_{r,x} - \angle E_{r,y} = \pm 90° \tag{7b}$$

then right-hand (+90°) or left-hand (-90°) CP radiation can be obtained for the reflected E-field.

The challenge here is how to evaluate the bandwidth of a unit cell for CP radiation based on the reflected magnitude and phase in (7). We know that the AR of a radiated wave is defined as [28]

$$AR = \sqrt{\frac{1 + M^2 + \sqrt{1 + M^4 + 2M^2\cos(2\phi)}}{1 + M^2 - \sqrt{1 + M^4 + 2M^2\cos(2\phi)}}} \tag{8}$$

where

$$M = |E_{r,x}|/|E_{r,y}| \tag{9a}$$

$$\text{and} \quad \phi = \angle E_{r,x} - \angle E_{r,y} \tag{9b}$$

Because the strong-reflected E-field can always have the condition of $|E_{r,x}| \to |E_{r,y}|$ (that also means $M \to 1$), we can calculate that, to meet the requirement of $AR \leq 3$ for the reflected wave, the reflected phase difference should be within the following relation.

$$70.5° \leq |\phi| \leq 109.5° \tag{10}$$

In this work, we will follow the relation in (10) to ensure that a good CP radiation (AR<3) can be obtained within the interested frequency bandwidth, when designing LP-CP unit cells for broadband CP array.

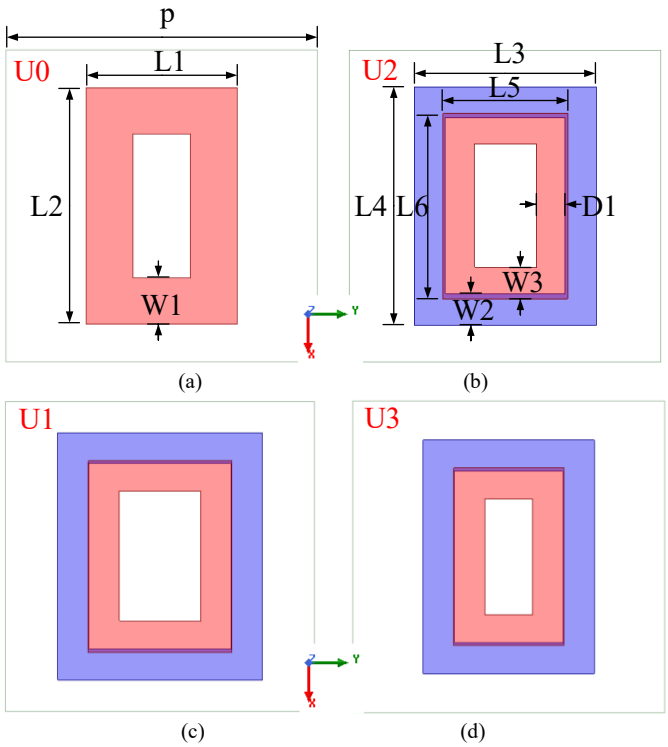

Fig. 8. Configurations of the 2-bit LP-CP unit cells. (a) Unit cell 0. (Detailed structure parameters: L1=4.85 mm, L2=7.6 mm, W1=1.5 mm). (b) Unit cell 2. (Detailed structure parameters: L3=5.85 mm, L4=7.65 mm, L5=4.0 mm, L6=6.0 mm, W2=1.0 mm, W3=1.0 mm, D1=0.9 mm.) (c) Unit cell 1. (Detailed structure parameters: L3=6.4 mm, L4=7.3 mm, L5=4.6 mm, L6=6.2 mm, W2=0.3 mm, W3=1.0 mm, D1=1.6 mm.) (d) Unit cell 3. (Detailed structure parameters: L3=5.5 mm, L4=7.5 mm, L5=3.5 mm, L6=5.7 mm, W2=1.0 mm, W3=1.0 mm, D1=0.9 mm.)

III. Unit Cells Realization

Based on the above theoretical illustrations, broadband LP-CP unit cells composed of single-loop and dual-loop are designed to achieve 2-bit phase delay in this section.

A. *Configuration*

Fig. 8 shows the detailed structures of the 2-bit unit cells. These unit cells are designed in a square lattice with the same period length (p=10 mm) working at the center frequency of 10 GHz. The layer configuration is the same as the previously discussed unit cells in Section II, including the substrates and

thickness. Detailed design parameters are listed in the caption of the figure. Note that unit cells U1 and U3 are originated from U2, so they share the same design parameter variables with U2. To achieve the desired phase shift of 70.5-109.5° between two orthogonal polarizations for CP radiation, the square loops have different lengths along x-axis and y-axis directions. Detailed design parameters are listed in the figure caption for designers' reference. In the figure, unit cell U0 is designed for the reference phase 0 at 10GHz, U1 is designed for reflective phase of -90°, U2 is designed for reflective phase of -180°, U3 is designed for reflective phase of -270°.

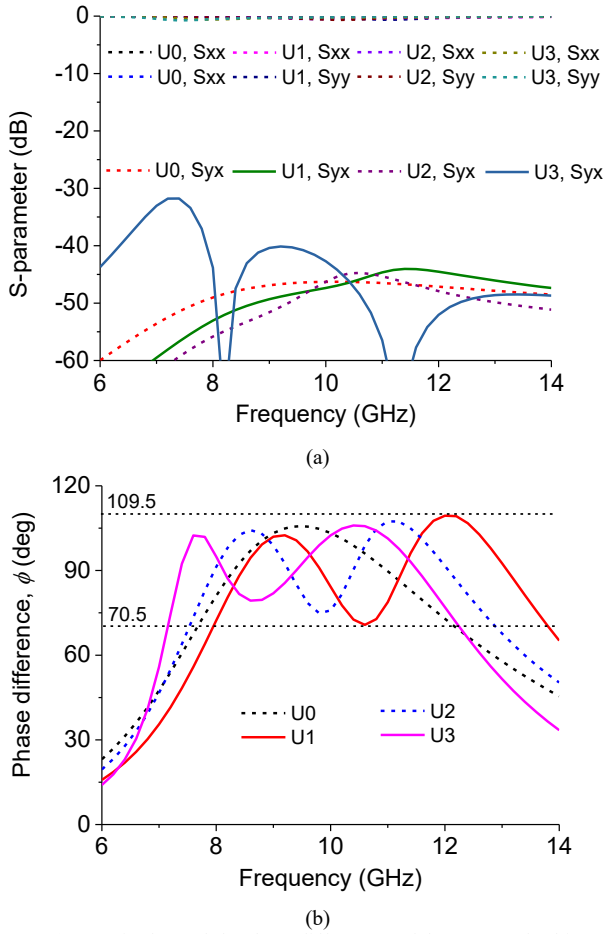

Fig. 9. (a) Magnitudes and (b) phase differences of the proposed 2-bit LP-CP unit cells.

B. Performance Investigation

The performances of the S-parameters for the proposed 2-bit LP-CP unit cells are shown in Fig. 9. First as shown in Fig. 9 (a), the reflection coefficients of four unit cells are very close to 0 dB for both x-axis and y-axis line-polarized waves. Eight curves of reflection coefficients are almost coincident to each other with the minimum value of around -0.6 dB. This proves that the condition of $|E_{r,x}| \rightarrow |E_{r,y}|$ is met in the whole interested band, so that we can use the phase relation in (10) to evaluate its CP bandwidth under the common requirement of AR<3 dB. In addition, it can be seen the transmission coefficients for the x-axis polarized wave into y-axis polarized wave are very low. This indicates that a high isolation or a low coupling is obtained for the incident waves illuminate the proposed 2-bit unit cells. It can be seen that the isolation is higher than 30 dB over the entire band.

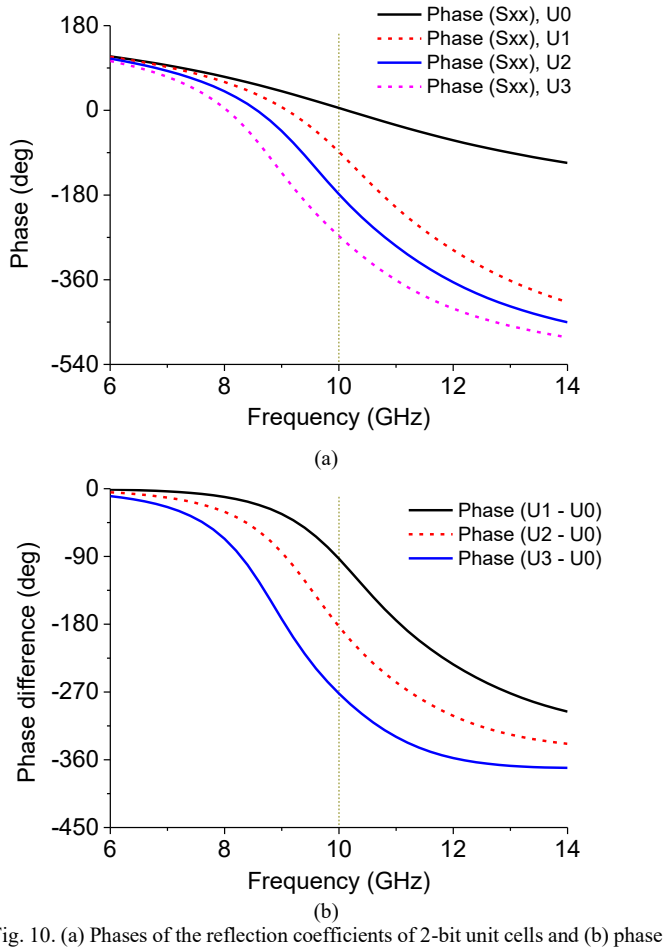

Fig. 10. (a) Phases of the reflection coefficients of 2-bit unit cells and (b) phase differences between different unit cells.

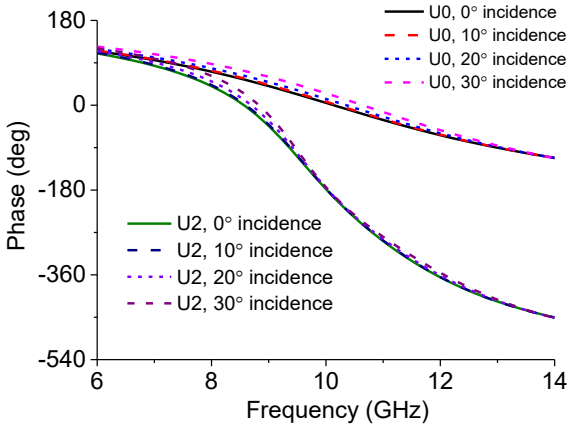

Fig. 11. Reflection phases of the unit cells under different incident angles.

The phase differences between the x-axis polarized wave and the y-axis polarized wave are shown in Fig. 9 (b). It can be seen that unit cell U0 has the narrowest phase bandwidth covering 7.67-12.18 GHz with only one phase peak. Unit cell U2 has the phase bandwidth covering 7.53-12.9 GHz, which is much wider than U0 because of the dual-loop structure. Two phase peaks are observed on the curve of unit cell U2. As discussed in Section II, by elaborately adjusting the structure parameters in U2, two different unit cells of U1 and U3 can be obtained for

±90° phase shift. So unit cells U1 and U3 have slight bandwidth shifts either to the left or right. The overlapped phase bandwidth of 70.5-109.5° of the four LP-CP unit cells is from 7.95 GHz to 12.18 GHz, which is aimed to evaluate the minimum CP bandwidth under the worst case when they are designed into RA aperture.

Fig. 10 shows the phase responses of the reflected phases of 2-bit unit cells for the x-axis polarized impinged wave. As shown in Fig. 10 (a), same as the illustration in Section II, the phase response of U0 is within [-180°, 180°], the phase responses of U1, U2, and U3 have a larger variance range within [-450°, 180°]. At the designed center frequency of 10 GHz, unit cells of U0, U1, U2, and U3 have the reflection phases of 0°, -90°, -180°, -270°, respectively. Therefore, a sequential phase difference of -90° is achieved in these four unit cells. Fig. 10 (b) shows the phase difference of unit cells U1, U2, and U3 relative to the first unit cell U0. It can be seen that the phase difference is changed in a negative gradient as the increase of the working frequency. The phase difference is -90° between U1 and U0, -180° between U2 and U0, and -270° between U3 and U0 at the designed center frequency. Owing to the similar dual-loop structure, the phase changing tendencies of these three unit cells are very similar, except with an elaborate bandwidth shift for different reflection phases.

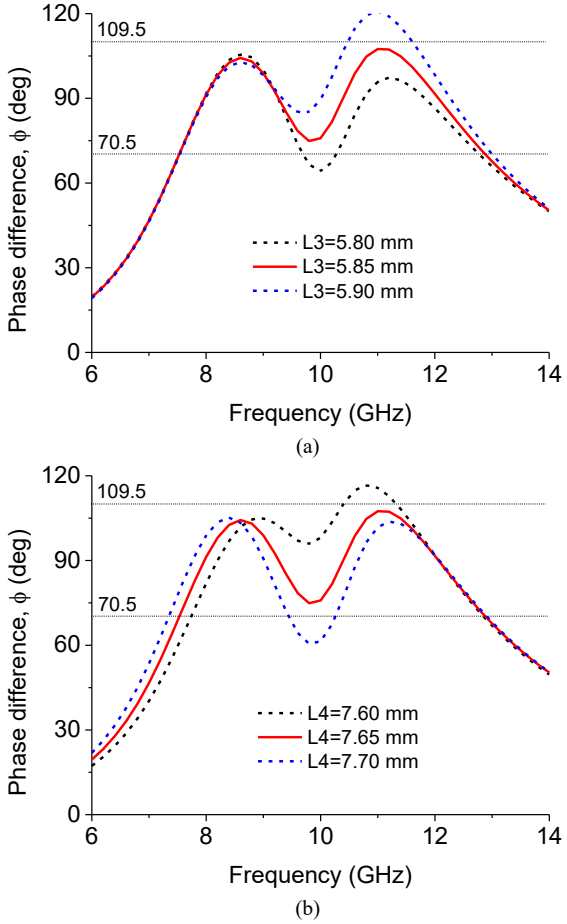

Fig. 12. Phasing bandwidth of the unit cell U2 varying with different parameters. (a) Width of outer loop (L3). (b) Length of the outer loop (L4).

The reflection phases of the unit cells under different incident angles are analyzed and shown in Fig. 11. Two representative results of single loop U0 and dual-loop U2 are given in the figure for a good comparison. It can be seen that both two unit cells show good consistence under different incident angles for the impinged wave. As the impinged wave changes from the normal direction to -30° direction, the reflection phase has a relatively large deviation as compared to reflection phase under normal incidence. The maximum phase variance is within 20° for unit cell U0, and the maximum phase variance is within 25° for unit cell U1. This denotes that a stable reflection phase can be achieved under different incidence for the proposed unit cells.

C. *Parametrical Studies*

When designing the proposed 2-bit unit cells, the phasing bandwidth is vital important to ensure the CP bandwidth of the RA. As dual-loop unit cell U2 has a wider phasing bandwidth and more complicated coupling structure, and unit cells U1 and U2 are developed based on this dual-loop structure, the key parameters in this structure are studied to provide the guidance for the design of broadband 2-bit LP-CP unit cells.

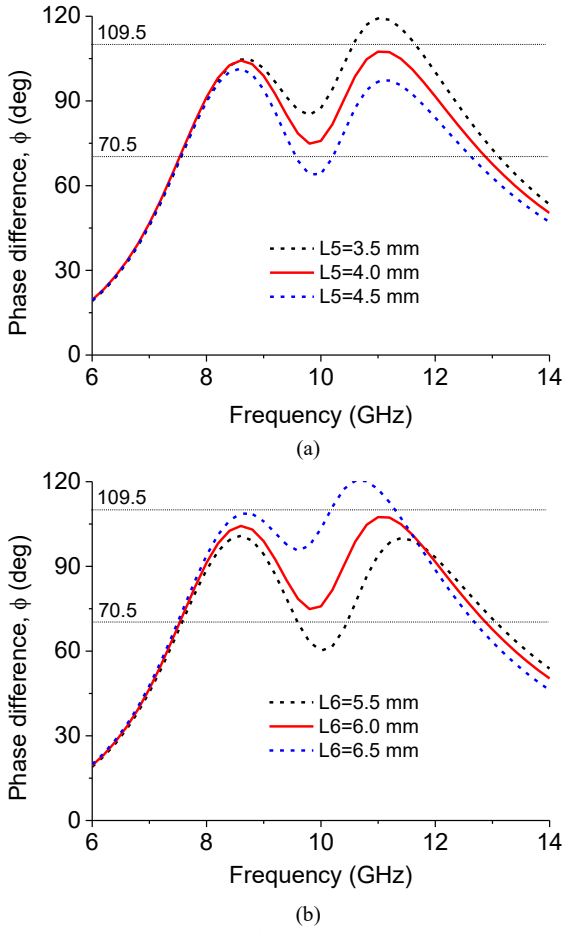

Fig. 13. Phasing bandwidth of the unit cell U2 varying with different parameters. (a) Width of inner loop (L5). (b) Length of the inner loop (L6).

Fig. 12 shows the phasing bandwidth (ϕ) of the unit cell U2 changing with the different widths (L3) and lengths (L4) of the outer loop. As shown in Fig. 12 (a), when the width is increased from 5.8 mm to 5.9 mm, only the band-edge at the upper frequency is shifted, and the bandwidth is therefore increased or narrowed. This can be utilized to adjust the phasing bandwidth in the upper frequency band. It can also be noticed

that as the width becomes narrower, more phase difference can be achieved between the x-axis and y-axis polarized waves, due to the increased difference in the structure of the outer loop. Fig. 12 (b) shows that the length (L4) of the outer loop has a great influence on the lower band-edge. As the length increases from 7.6 mm to 7.7 mm, the lower band-edge shifts to the lower frequency. The phase difference between two orthogonal polarizations is reduced accordingly. When the length reduces, the lower band-edge shifts to the upper frequency with the phase difference increased. It can also be found that the upper band-edge is nearly unaffected by this parameter. The width (L3) and length (L5) have their respective influences either on the upper or lower band-edges.

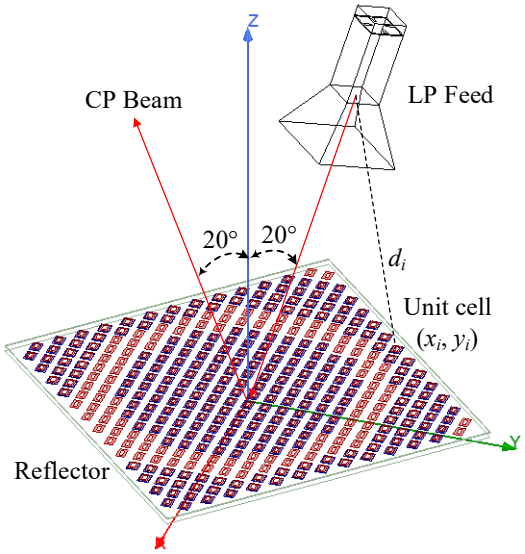

Fig. 14. 3D view of the proposed LP-CP RA.

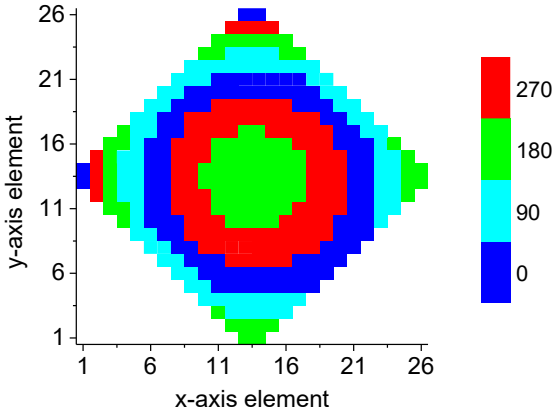

Fig. 15. Discretized phase distributions of unit cells in the developed 2-bit LP-CP RA.

The effects of the parameters of the inner loop in unit cell U2 are shown in Fig. 13. First as shown in Fig. 13 (a), the width of the inner loop (L5) has a very similar changing tendency as the width of the outer loop (L3). When L5 increases, less phase difference is obtained between the two orthogonal polarizations due to the reduced structure difference in two orthogonal directions. In addition, if more phase difference is wanted, L5 should be reduced accordingly. Fig. 13 (b) shows the effect of the length of the inner loop (L6) on the performance of the phasing bandwidth. It can be seen that the variance of L6 also has an important influence on the upper band-edge of the phasing bandwidth. As L6 increases from 5.5 mm to 6.5 mm, the upper band-edge moves to lower frequency slightly. This causes more phase difference is achieved due to the increase structure difference in two orthogonal directions. It is also noticed that both the width and length of the inner loop can have large influences on the upper band-edge, while have little influences on the lower band-edge. According to the above clear and effective parametrical studies and the bandwidth shift effects, it will not be difficult to develop the remaining 2-bit LP-CP unit cells by elaborately adjusting the widths and lengths of the outer and inner loops.

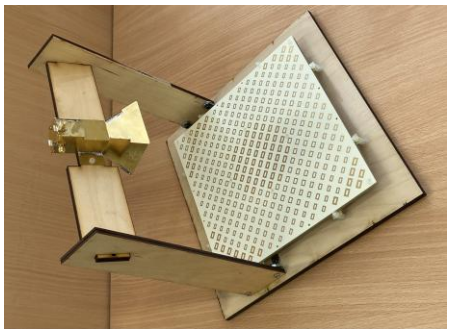

Fig. 16. Photographs of the fabricated 2-bit LP-CP RA.

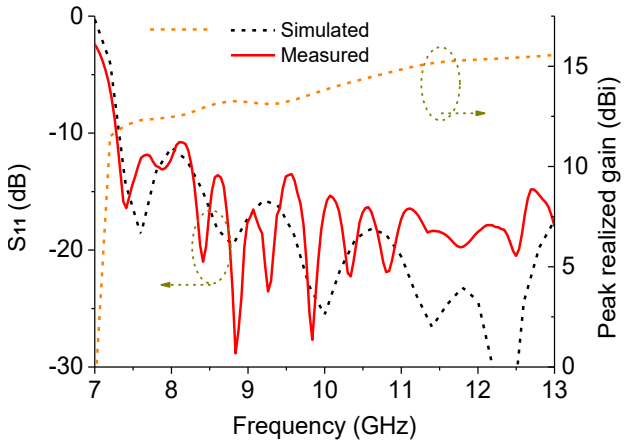

Fig. 17. Measured and simulated S_{11} and gain of the feed horn.

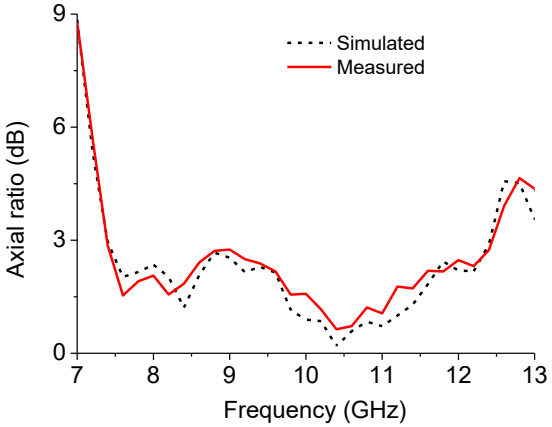

Fig. 18. Measured and simulated AR of the developed LP-CP RA.

IV. CP Reflectarray Design

Based on the above design of the 2-bit unit cells, a broadband LP-CP RA in a square aperture with the total elements of 364

elements is developed, fabricated, and measured for high gain satellite IoV in this section.

A. Array Configuration

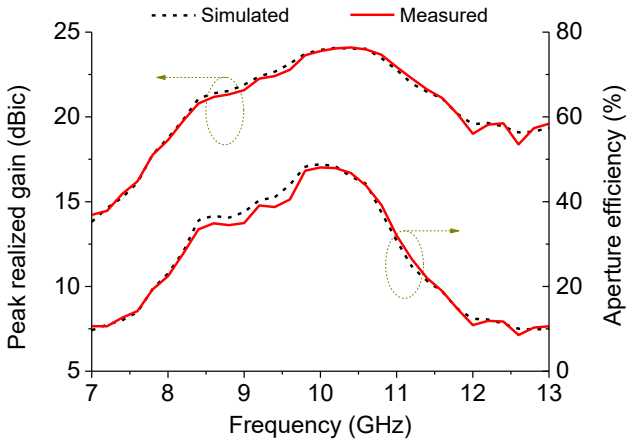

Fig. 19. Measured and simulated peak realized gains and aperture efficiencies of the developed LP-CP RA.

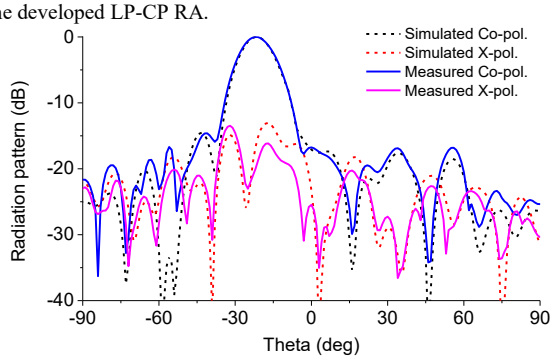

(a)

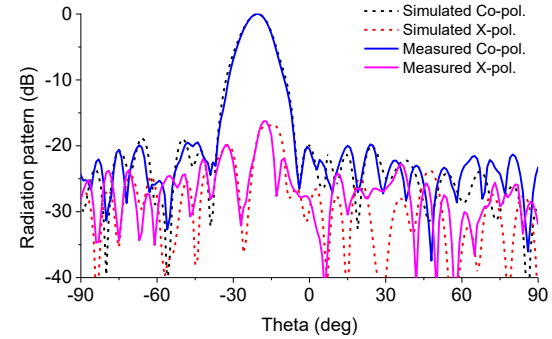

(b)

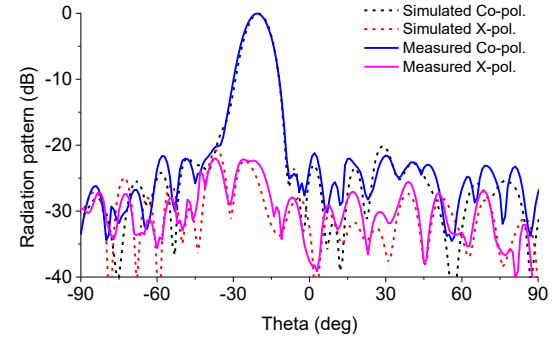

(c)

Fig. 20. Normalized radiation patterns of the proposed 2-bit LP-CP RA in φ=-45° plane at (a) 8 GHz, (b) 10 GHz, and (c) 12 GHz.

Fig. 14 shows the 3D view of the designed broadband LP-CP RA. As can be seen, to realize high gain CP radiation, a LP horn antenna as the feed source is located above the LP-CP reflector with the focal length of 180 mm. A focal to diameter ratio (f/D) of 0.9 is selected, which aims to maintain a high aperture efficiency (AE) balance for both high illumination and low spillover within the operation bandwidth. To avoid the possible blockage of the feed, the horn is designed with 20° offset, while the beam direction is designed with an opposite symmetrical -20° offset. It should be noticed that both the feed and the beam direction are arranged in the φ=-45° plane for the convenience of the installation of the horn antenna above the square reflector surface. The length and width directions of the unit cells are in x-axis and y-axis, and the polarization direction of the horn antenna is in the φ=-45° plane for right-hand CP radiation, or in the φ=45° plane for left-hand CP radiation.

To realize high gain CP radiation in the desired beam direction of (θ, φ) = (-20°, -45°) as shown in the figure, we need to calculate the required phase delay for each unit cell (ϕ_R) based on the below equation [21],

$$\phi_R = k_0(d_i - (x_i cos\varphi_b + y_i sin\varphi_b)sin\theta_b) + \phi_0 \quad (11)$$

where k_0 is the propagation constant in vacuum, d_i is the distance of the phase center of the feed to the unit cell i, (x_i, y_i) is the coordinate of unit cell i, and (θ_b, φ_b) is the array beam direction, ϕ_0 is a compensated constant phase for all the unit cells. Because the designed LP-CP unit cells are not in a continuous phase change, the calculated phase needs to be discretized into 2-bit form with a stepped 90° phase difference. In this design, the discretized 2-bit phase distribution working at 10 GHz is calculated and shown in Fig. 15 for the design of the developed LP-CP RA.

B. Results

The designed 2-bit LP-CP RA was then fabricated and measured at Brunel University London and the University of Kent. Fig. 16 shows the photographs of the fabricated CP RA prototype. The measured and simulated impedance bandwidths and gain of the feed horn are shown in Fig. 17. Aa can be seen, the measured S_{11} agrees well with the simulated result with a slight frequency shift. The measured impedance bandwidth for S_{11}<10 dB covers 7.28-13 GHz. The simulated peak realized gain varies almost linearly from 12 dBi to 15.5 dBi. The broad impedance bandwidth and linear radiation performance can ensure a uniform and efficient illumination to the RA aperture.

The measured AR in the beam direction is shown in Fig. 18, and the simulated result is added for comparison. It can be seen that a good agreement is achieved between the simulated and measured results, and the AR bandwidth also has a reasonable agreement with the phasing bandwidth of the overlapped phasing bandwidth of the 2-bit unit cells. The CP bandwidth for AR<3 dB is from 7.3 GHz to 12.5 GHz (52.5%), which has a slight frequency shift to the upper frequency. The measured result confirms that a broad AR bandwidth can be utilized for satellite X-band IoV coverage.

The measured peak realized gain is shown in Fig. 19, and the measured aperture efficient is also added in this figure, which is calculated based on the measured peak realized gain. As can be seen the measured peak realized gain and aperture efficiency have a good accordance with the tendency of the simulated gain

and efficiency curves. The measured maximum peak realized gain is 24.1 dBic at 10.2 GHz. Its measured 3 dB gain bandwidth covers from 8.4 GHz to 11.6 GHz (32%). By using the measured peak realized gain, the calculated maximum AE is 48% at 10 GHz. The measured AE>30% bandwidth covers 8.3 GHz to 11.1 GHz. The high gain and AE within the bandwidth can ensure the high sensitivity and low latency communication for IoV vehicles.

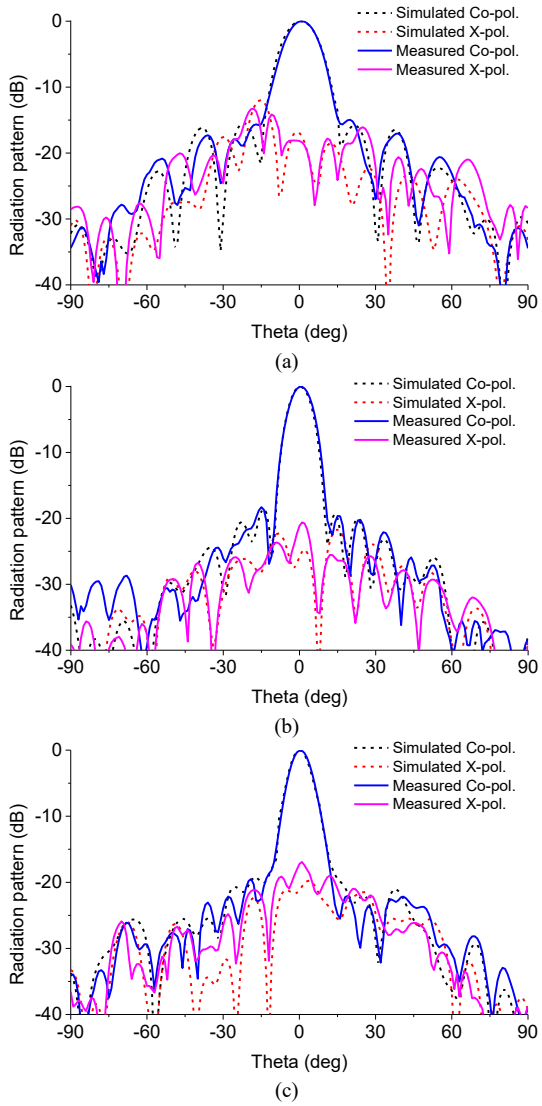

Fig. 21. Normalized radiation patterns of the proposed 2-bit LP-CP RA in the other orthogonal plane to φ=-45° (in beam direction) at (a) 8 GHz, (b) 10 GHz, and (c) 12 GHz.

The measured normalized radiation patterns in two orthogonal planes in the beam direction are shown in Fig. 20 and Fig. 21. Fig. 20 gives the φ=-45° plane radiation patterns at 8 GHz, 10 GHz, and 12 GHz. Note that in the figure, the co-polarized radiation patterns are in right-hand CP radiation, and the cross-polarized radiation patterns are in left-hand CP radiation. It can be seen that the measured radiation patterns are in good accordance with the simulated results. Beams with -20° incline are achieved just as predicted by the simulated results. The half-power beamwidth changes from 15° to 10° within the bandwidth, and the sidelobe levels are around 14.6 dB lower than the main lobe.

The measured radiation patterns in the orthogonal plane to φ=45° at 8 GHz, 10 GHz, and 12 GHz are shown in Fig. 21. It can be seen that nearly symmetrical co-polarized radiation patterns are achieved in this plane. Maximum radiation is realized in the center of the observing range. The measured sidelobe levels are around 14.9 dB lower than the main beam. In addition, the half-power beamwidth is around 12° to 8° within bandwidth. Overall, relatively a good accordance is achieved between the measured and the simulated radiation patterns. The main discrepancies between the measured and simulated results are from the manufacture errors and assembly errors in the antenna fabrication, and the position errors in the radiation patterns measurement.

C. *Comparison*

The advantages of the performances of our developed CP RA are compared and listed in Table I. Note that to be a fair performance comparison considering different types of array antennas, only recently developed LP-CP RAs are compared in the table. In the table, λ_0 is the free-space wavelength at the center frequency. Compared to [22]-[25], it is obvious that our developed RA has a much wider gain and AR bandwidth even with a thinner thickness of the relative reflective surface. It is worth pointing that, [27] has a very thick overall due to the idea of using 3D printed dielectric slab for reflective phasing control. Owing to the use of low permittivity and thin substrate, high-Q RA is achieved in [23] with a high peak AE but a narrow bandwidth. In a good comparison, [25] have much closer thicknesses as our design. Owing to the introduction of the novel wideband LP-CP unit cells, our designed RA has an obviously wider gain bandwidth of 32% and AR bandwidth of 53%, with thin aperture thickness of $0.11\lambda_0$ and high peak AE of 48%. Such a planar broadband high gain RA can provide high throughput and low latency communications for different vehicles in satellite IoV service.

TABLE I
COMPARISON OF THE RECENTLY DEVELOPED LP-CP RAS

Ref.	3dB gain BW	AR BW	Thickness (λ_0)	Aperture $\lambda_0\times\lambda_0$	F/D	Peak gain (dBic)	Peak AE
[22]	4%	3.3%	0.26	5.3×5.3	0.6	21.6	41%
[23]	11%	10%	0.05	π×14×14	0.62	36.7	66.5%
[24]	26.5%	39%	0.2	7×7	0.71	23.5	42%
[25]	12.8%	12.5%	0.11	5.4×5.4	1.2	20.38	30%
[27]	28.3%	40.2%	2.19	10.6×10.6	1.55	27.9	38%
This work	32%	53%	0.11	6.4×6.4	0.9	24.1	48%

V. CONCLUSION

This paper proposes a novel method of realizing broadband CP RA for satellite IoV applications. In detail, single loop and dual-loop structured LP-CP unit cells are utilized for stepped 0, -90°, -180°, and -270° reflective phase delays. The inner working principle is illustrated by equivalent circuits, related derivation, and both theoretical and simulated results. In

addition, a phase bandwidth to ensure CP radiation bandwidth is proposed as the baseline for designing LP-CP unit cells. Therefore, broadband CP radiation can be guaranteed for the designed CP RA. Finally, the proposed unit cells are utilized in designing RA for high gain CP radiation. Both the simulated and measured results show that the developed CP RA can have a broad 3dB gain bandwidth of 32% and 3dB AR bandwidth of 53%. In addition, high peak AE of 48% is achieved with a low aperture thickness of $0.11\lambda_0$. The low fabrication cost, simple structure, thin thickness aperture, and broad bandwidths in impedance and CP radiation demonstrate the feasibility of the developed CP RA in providing broadband connection in satellite IoV application.

REFERENCES

[1] E. Kim, I. P. Roberts and J. G. Andrews, "Downlink analysis and evaluation of multi-beam LEO satellite communication in shadowed rician channels," *IEEE Trans. Veh. Technol.*, vol. 73, no. 2, pp. 2061-2075, Feb. 2024.

[2] B. J. Xiang, X. Dai and K. -M. Luk, "A wideband 2-bit transmitarray antenna for millimeter-wave vehicular communication," *IEEE Trans. Veh. Technol.*, vol. 71, no. 9, pp. 9202-9211, Sept. 2022.

[3] Z. Wang, S. Liu and Y. Dong, "Compact wideband pattern reconfigurable antennas inspired by end-fire structure for 5G vehicular communication," *IEEE Trans. Veh. Technol.*, vol. 71, no. 5, pp. 4655-4664, May 2022.

[4] Z. -X. Xia, K. W. Leung, P. Gu and R. Chen, "3-D-printed wideband high-efficiency dual-frequency antenna for vehicular communications," *IEEE Trans. Veh. Technol.*, vol. 71, no. 4, pp. 3457-3469, April 2022.

[5] Y. -F. Cheng, Y. -X. Wang, J. -L. Zhong, C. Liao and X. Ding, "Shared-metasurface antenna with diverse reflection, radiation and polarization characteristics for vehicular communications," *IEEE Trans. Veh. Technol.*, vol. 72, no. 6, pp. 7573-7583, June 2023.

[6] Z. Zhang, S. -W. Wong, Y. Wen, S. -Q. Zhang, W. Li and Y. He, "A full-metal dual-band millimeter-wave antenna array with concomitant multifold orthogonal beamforming for V2V and V2I communications," *IEEE Trans. Veh. Technol.*, vol. 73, no. 7, pp. 10381-10389, July 2024.

[7] Y. Zhang, J. -Y. Deng, D. Sun, J. -Y. Yin and L. -X. Guo, "Compact slow-wave SIW h-plane horn antenna with increased gain for vehicular millimeter wave communication," *IEEE Trans. Veh. Technol.*, vol. 70, no. 7, pp. 7289-7293, July 2021.

[8] C. Wang, W. Cao, W. Ma, Y. Tong and Y. Zhu, "A sigle-layer dual-band shared-aperture antenna with high gain and sidelobe suppression based on high-order mode for vehicular communications," *IEEE Trans. Veh. Technol.*, vol. 73, no. 1, pp. 473-481, Jan. 2024.

[9] L. Wen, S. Gao, Q. Luo, W. Hu and Y. Yin, "Wideband dual circularly polarized antenna for intelligent transport systems," *IEEE Trans. Veh. Technol.*, vol. 69, no. 5, pp. 5193-5202, May 2020.

[10] L. Wen et al., " A wideband series-fed circularly polarized differential antenna by using crossed open slot-pairs," *IEEE Trans. Antennas Propag.*, vol. 68, no. 4, pp. 2565-2574, April 2020.

[11] J. -D. Zhang, W. Wu and D. -G. Fang, "Dual-band and dual-circularly polarized shared-aperture array antennas with single-layer substrate," in *IEEE Trans. Antennas Propag.*, vol. 64, no. 1, pp. 109-116, Jan. 2016.

[12] J. Ran, Y. Wu, C. Jin, P. Zhang and W. Wang, "Dual-band multipolarized aperture-shared antenna array for Ku-/Ka-band satellite communication," *IEEE Trans. Antennas Propag.*, vol. 71, no. 5, pp. 3882-3893, May 2023.

[13] J. Li, Y. Hu, L. Xiang, W. Kong and W. Hong, "Broadband circularly polarized magnetoelectric dipole antenna and array for K-band and Ka-band satellite communications," *IEEE Trans. Antennas Propag.*, vol. 70, no. 7, pp. 5907-5912, July 2022.

[14] R. S. Hao, J. F. Zhang, S. C. Jin, D. G. Liu, T. J. Li and Y. J. Cheng, "K-/Ka-band shared-aperture phased array with wide bandwidth and wide beam coverage for LEO satellite communication," *IEEE Trans. Antennas Propag.*, vol. 71, no. 1, pp. 672-680, Jan. 2023.

[15] Z. -J. Guo, Z. -C. Hao, H. -Y. Yin, D. -M. Sun and G. Q. Luo, "Planar shared-aperture array antenna with a high isolation for millimeter-wave low earth orbit satellite communication system," *IEEE Trans. Antennas Propag.*, vol. 69, no. 11, pp. 7582-7592, Nov. 2021.

[16] Q. Luo et al., "Multibeam dual-circularly polarized reflectarray for connected and autonomous vehicles," *IEEE Trans. Veh. Technol.*, vol. 68, no. 4, pp. 3574-3585, April 2019.

[17] J. Zhu, S. Liao, X. Zhu, Y. Yang and Q. Xue, "C-/Ka-band aperture-shared dual circularly polarized heterogeneous reflectarray for vehicular communications," *IEEE Trans. Veh. Technol.*, vol. 73, no. 6, pp. 8671-8680, June 2024.

[18] L. Zhang et al., "A single-layer 10–30 GHz reflectarray antenna for the internet of vehicles," *IEEE Trans. Veh. Technol.*, vol. 71, no. 2, pp. 1480-1490, Feb. 2022.

[19] L. Zhang, S. Gao, Q. Luo, W. Li, Y. He and Q. Li, "Single-layer wideband circularly polarized high-efficiency reflectarray for satellite communications," *IEEE Trans. Antennas Propag.*, vol. 65, no. 9, pp. 4529-4538, Sept. 2017.

[20] M. Veljovic and A. K. Skrivervik, "Ultralow-profile circularly polarized reflectarray antenna for cubesat intersatellite links in K-band," *IEEE Trans. Antennas Propag.*, vol. 69, no. 8, pp. 4588-4597, Aug. 2021.

[21] L. Wen, S. Gao, Q. Luo, W. Hu, B. Sanz-Izquierdo, and X. -X. Yang, "Wideband circularly polarized reflectarray antenna using rotational symmetrical crossed dipoles," *IEEE Trans. Antennas Propag.*, vol. 71, no. 5, pp. 4576-4581, May 2023.

[22] D. Kundu, A. Parameswaran, H. S. Sonalikar, D. Bhattacharya and S. Gupta, "A low-RCS circularly polarized reflectarray antenna with a linearly polarized feed," *IEEE Trans. Antennas Propag.*, vol. 71, no. 8, pp. 6501-6512, Aug. 2023.

[23] R. Deng, Y. Mao, S. Xu and F. Yang, "A single-layer dual-band circularly polarized reflectarray with high aperture efficiency," *IEEE Trans. Antennas Propag.*, vol. 63, no. 7, pp. 3317-3320, July 2015.

[24] Q. Zhou and L. Guo, "A multipolarized metal-only reflectarray antenna," *IEEE Trans. Antennas Propag.*, vol. 71, no. 8, pp. 6977-6982, Aug. 2023.

[25] S. R. Lee, E. H. Lim, F. L. Lo and W. H. Ng, "Circularly polarized elliptical microstrip patch reflectarray," *IEEE Trans. Antennas Propag.*, vol. 65, no. 8, pp. 4322-4327, Aug. 2017.

[26] D. R. Prado, P. Naseri, J. A. López-Fernández, S. V. Hum and M. Arrebola, "Support vector regression-enabled optimization strategy of dual circularly-polarized shaped-beam reflectarray with improved cross-polarization performance," *IEEE Trans. Antennas Propag.*, vol. 71, no. 1, pp. 497-507, Jan. 2023.

[27] Q. Cheng et al., "Dual circularly polarized 3-D printed broadband dielectric reflectarray with a linearly polarized feed," *IEEE Trans. Antennas Propag.*, vol. 70, no. 7, pp. 5393-5403, July 2022.

[28] L. Wen, S. Gao, Q. Luo, W. Hu, and B. Sanz-Izquierdo, "Design of a broadband circularly polarized antenna by using axial ratio contour," *IEEE Antennas Wirel. Propag. Lett.*, vol. 19, no. 12, pp. 2487-2491, Dec. 2020.